

Miscible displacements in Hele-Shaw cells: three-dimensional Navier–Stokes simulations

Rafael M. Oliveira and Eckart Meiburg†

Department of Mechanical Engineering, University of California at Santa Barbara, Santa Barbara,
CA 93106, USA

(Received 7 February 2011; revised 2 August 2011; accepted 30 August 2011;
first published online 12 October 2011)

Three-dimensional Navier–Stokes simulations of viscously unstable, miscible Hele-Shaw displacements are discussed. Quasisteady fingers are observed whose tip velocity increases with the Péclet number and the unfavourable viscosity ratio. These fingers are widest near the tip, and become progressively narrower towards the root. The film of resident fluid left behind on the wall decreases in thickness towards the finger tip. The simulations reveal the detailed mechanism by which the initial spanwise vorticity of the base flow, when perturbed, gives rise to the cross-gap vorticity that drives the fingering instability in the classical Darcy sense. Cross-sections at constant streamwise locations reveal the existence of a streamwise vorticity quadrupole along the length of the finger. This streamwise vorticity convects resident fluid from the wall towards the centre of the gap in the cross-gap symmetry plane of the finger, while it transports injected fluid laterally away from the finger centre within the mid-gap plane. In this way, it results in the emergence of a longitudinal, inner splitting phenomenon some distance behind the tip that has not been reported previously. This inner splitting mechanism, which leaves the tip largely intact, is fundamentally different from the familiar tip-splitting mechanism. Since the inner splitting owes its existence to the presence of streamwise vorticity and cross-gap velocity, it cannot be captured by gap-averaged equations. It is furthermore observed that the role of the Péclet number in miscible displacements differs in some ways from that of the capillary number in immiscible flows. Specifically, larger Péclet numbers result in wider fingers, while immiscible flows display narrower fingers for larger capillary numbers. Furthermore, while higher capillary numbers are known to promote tip-splitting, inner splitting is delayed for larger Péclet numbers.

Key words: fingering instability, Hele-Shaw flows

1. Introduction

The formation of viscous fingers in Hele-Shaw displacements has been an active research area for over half a century, following the pioneering studies by Hill (1952), Saffman & Taylor (1958) and Chuoke, van Meurs & van der Poel (1959); see the review by Homsy (1987). This classical instability phenomenon is of importance in numerous application areas, including oil recovery processes, hydrology, small-scale MEMS devices, and pattern formation.

† Email address for correspondence: meiburg@engineering.ucsb.edu

Initially, the majority of investigations addressed immiscible displacements, and their dependence on the capillary number. It was perhaps tacitly assumed that miscible displacements behaved in a qualitatively similar fashion, with the Péclet number playing a role comparable to that of the capillary number in immiscible flows. Among the first to focus explicitly on the effects of miscibility and diffusion was the study by Wooding (1969). The author pointed out the existence of an initial, diffusion-dominated phase, followed by a subsequent convection-dominated regime. More recent investigations found that the dominant wavelength of well-developed, nonlinear fingers is typically of the order of three (microgravity experiments, Aubertin *et al.* 2009), four (radial displacements, Paterson 1985) or five (vertical Hele-Shaw cell with density difference, Lajeunesse *et al.* 1997) times the gap width of the Hele-Shaw cell.

Traditionally, Darcy's law has been employed to explore the fundamental dynamics of these fingering instabilities. However, in recent years a number of alternative approaches have led to interesting comparisons with Darcy-based predictions. Rakotomalala, Salin & Watzky (1997*a,b*) use BGK lattice gas simulations to calculate the two-dimensional dynamics of miscible displacement fronts within the gap of Hele-Shaw cells, as a function of the Péclet number and mobility ratio.

In the linear regime, Fernandez *et al.* (2002) experimentally determined dispersion relations for miscible Rayleigh–Taylor instabilities in vertical Hele-Shaw cells. The corresponding linear stability analysis by Graf, Meiburg & Härtel (2002), based on the three-dimensional Stokes equations, observes good agreement with the experimental growth rates across five orders of magnitude in the Rayleigh number. These authors also compare the Stokes-based dispersion relations with corresponding results derived from a gap-averaged Darcy approach, and they find reasonable agreement only for moderate Rayleigh numbers. For large values of this parameter, the three-dimensional flow structure within the gap becomes important, so that averaging across the gap can no longer capture the dominant physical mechanisms. The same problem was also investigated by Martin, Rakotomalala & Salin (2002), who employed a gap-averaged Navier–Stokes–Darcy equation to obtain dispersion relations for the Rayleigh–Taylor instability that compare favourably to three-dimensional lattice BGK simulations. Along similar lines, Zeng, Yortsos & Salin (2003) considered a modification of the Brinkman correction to Darcy's equation for gravitationally and pressure-driven displacements. Additional Stokes-based linear stability results for chemically reacting and variable viscosity Hele-Shaw displacements were discussed by Demuth & Meiburg (2003), Goyal & Meiburg (2004, 2006), Schafroth, Goyal & Meiburg (2007) and Goyal, Pichler & Meiburg (2007), showing similar discrepancies between Stokes-based and gap-averaged results.

It is clear that the Darcy-based modelling approach has been very successful in reproducing several important phenomena that had been observed experimentally for miscible Hele-Shaw displacements. For example, the early linear stability investigations by Tan & Homsy (1986) show that increasing unfavourable viscosity ratios result in larger growth rates and shorter wavelengths of the most unstable mode, which is consistent with experimental data. The subsequent nonlinear simulations by Tan & Homsy (1988) were able to reproduce the tip-splitting phenomenon, and they explained the physical mechanism responsible for it. Nevertheless, the above observations in the context of more recent, Stokes-based linear stability analyses hint at the limitations of analysing instability phenomena in Hele-Shaw flows based on Darcy's law. Conversely, they raise the question of how accurately Darcy-type porous media displacements can be modelled by corresponding Hele-Shaw flows. The present investigation intends to shed some light on these issues in the nonlinear regime, by

focusing on the evolution of quasisteady fingers and their subsequent instabilities. In particular, we will focus on the role of the cross-gap velocity and the streamwise vorticity component, neither one of which can be captured by gap-averaged equations. It will be seen that in miscible displacements both of these quantities are important, and that they lead to a fundamentally new finger-splitting phenomenon that had not been identified previously.

As a second focus, the present investigation will compare the role of the Péclet number in miscible displacements to that of the capillary number in their immiscible counterparts. We will see that with regard to some flow features, these parameters play corresponding roles. However, in other respects, their influence can be opposite in nature.

The remainder of this paper is organized as follows. Section 2 describes the physical problem and formulates the governing equations, while §3 presents the details of the direct numerical simulation (DNS) approach. It also briefly discusses the parallelization of the computational code, along with validation results. Section 4 focuses on the nonlinear evolution of viscous fingers, on their quasisteady shapes, and on potential subsequent instabilities, as functions of the Péclet number and viscosity ratio. A novel ‘inner splitting’ phenomenon is identified, which is subsequently addressed in more detail in §5. Here, the mechanism behind this new instability will be explored, and particular attention will be drawn to the roles of the cross-gap velocity and streamwise vorticity in this regard. Section 6 will focus specifically on the vorticity dynamics of the flow. It will identify the mechanisms by which the purely spanwise vorticity of the Poiseuille-type base flow, when perturbed, partially reorients itself through tilting and viscous reconnection. In this way, it leads to emergence of the cross-gap vorticity that drives the fingering instability in the classical, gap-averaged Darcy sense. Sections 7 and 8, focus on comparisons of miscible versus immiscible displacements, and of Navier–Stokes versus Darcy results, respectively. Section 9 summarizes the main findings of the present investigation.

2. Physical problem

We consider two miscible fluids of different viscosities confined between two horizontal parallel plates separated by a gap of width b (see figure 1). The less viscous fluid with viscosity μ_1 displaces the more viscous fluid with viscosity μ_2 , giving rise to fingering instabilities. We will analyse these instabilities via numerical simulations of the three-dimensional, incompressible Navier–Stokes equations coupled to a convection–diffusion equation for the concentration field. Consistent with previous authors (e.g. Tan & Homsy 1986; Goyal & Meiburg 2006) we assume the constitutive relation between viscosity and concentration to be of exponential form:

$$\mu = \mu_1 e^{Mc}, \quad M = \ln \frac{\mu_2}{\mu_1}. \quad (2.1)$$

Here, c denotes the relative concentration of the more viscous fluid, and M is the viscosity ratio. To render the variables in a dimensionless form, we scale lengths by the gap width b , viscosities by the smaller viscosity μ_1 , and velocities by the gap-averaged inflow velocity U . The characteristic time is b/U , and the characteristic pressure is defined as $\mu_1 U/b$. Thus, our governing equations in terms of non-dimensional variables read

$$\frac{\partial u_k}{\partial x_k} = 0, \quad (2.2)$$

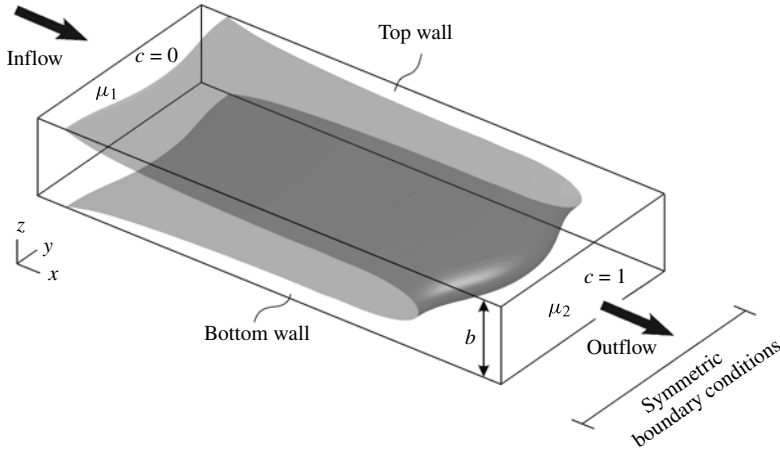


FIGURE 1. Schematic figure showing the geometry of the problem. The less viscous fluid with viscosity μ_1 displaces a more viscous fluid with viscosity μ_2 , in a Hele-Shaw cell of gap width b .

$$\frac{\partial u_i}{\partial t} + u_k \frac{\partial u_i}{\partial x_k} = \frac{1}{Re} \left[\frac{\partial}{\partial x_k} \mu \left(\frac{\partial u_i}{\partial x_k} + \frac{\partial u_k}{\partial x_i} \right) - \frac{\partial p}{\partial x_i} \right], \quad (2.3)$$

$$\frac{\partial c}{\partial t} + u_k \frac{\partial c}{\partial x_k} = \frac{1}{Pe} \frac{\partial}{\partial x_k} \frac{\partial c}{\partial x_k}. \quad (2.4)$$

Index notation is employed for the above set of equations, which represent the conservation of mass, momentum and species, respectively, with $u_i = (u, v, w)$ indicating the flow velocity; p denotes pressure, and t time. A traditional Cartesian coordinate system $x_k = (x, y, z)$ is used, with x denoting the streamwise direction, while y and z indicate the spanwise and cross-gap directions, respectively.

We have three main dimensionless parameters governing the dynamics, namely the viscosity ratio M , the Reynolds number Re , and the Péclet number Pe . The latter two are defined by

$$Re = \frac{\rho Ub}{\mu_1}, \quad Pe = \frac{Ub}{D}, \quad (2.5)$$

and indicate the relative strength of convective-to-diffusive transport in the momentum and species conservation equations, respectively. The simulations to be described below will address the low-Reynolds-number regime, and consequently we will employ $Re = 1$ throughout. We will primarily analyse the influence of M and Pe on the growth of quasisteady fingers, and on any subsequent instabilities of these fingers.

3. Numerical approach

We follow Rai & Moin (1991) and use finite differences in a three-step hybrid Runge–Kutta/Crank–Nicolson discretization to solve (2.2)–(2.4). The approach employs an explicit Runge–Kutta (RK) method for the convective terms, along with an implicit Crank–Nicolson method for the viscous terms. The discretization is second-order accurate in time for the viscous terms and third-order for the convective terms, the overall accuracy being second-order in time. The fractional step method employed takes advantage of a projection method that makes use of old values of the pressure

gradient in the momentum equations to solve for the corrector term in each step of the RK iteration. In addition, the divergence-free condition is not solved directly, but is combined with the corrector step to obtain a Poisson equation for ϕ , a scalar related to pressure. A factorization approximation is used when solving the linear system resultant of the diffusive integration, which reduces the memory requirements, and allows us to solve three tridiagonal systems instead of inverting a large sparse matrix (Kim & Moin 1985).

The above discretization uses second-order central differences on a uniform staggered grid to compute the viscous terms, the divergence of the velocity field, and the gradients of pressure and ϕ . The derivatives of the convective terms are calculated using the fifth-order Hamilton–Jacobi weighted essentially non-oscillatory (HJ WENO) scheme of Jiang & Peng (2000), as described by Osher & Fedkiw (2003).

The Poisson equation is solved using transform methods, as suggested by Kim & Moin (1985). Following those authors, we take the cosine transform of ϕ in both directions perpendicular to the flow direction, use the orthogonality property of cosines, and obtain a second-order ordinary differential equation for the transformed variable, which is discretized using central differences and solved in parallel via Gaussian elimination (Qin & Nguyen 1998). The solution ϕ is then readily obtained by taking the inverse transform. The implementation of the transform methods is straightforward using an open implementation of fast Fourier transforms sequentially in both the y - and z -directions. Once ϕ is obtained, the last step of the fractional step methods is performed to obtain the corrected velocity. The last stage in each step of the RK iteration is to update the pressure gradient field in terms of the scalar ϕ and old values of the pressure gradient. The code is parallelized using message passing interface (Pacheco 1997) through a domain decomposition along the flow direction. This requires communicating data across a total of six layers of ghost nodes at the upstream and downstream boundaries of each subdomain.

At the walls, we require all velocity components and the normal derivative of the concentration to vanish. At the spanwise boundaries, Neumann symmetry conditions are enforced in these four variables. The Navier–Stokes equations require no *a priori* boundary conditions on the pressure, since boundary conditions applied to the momentum equations suffice to allow for the determination of both velocity and pressure (Gresho & Sani 1987). For the staggered grid configuration employed here, the no-slip condition at the walls implies that the normal pressure gradient also vanishes at the walls. The choice of a cosine transform to solve the Poisson equation for ϕ is consistent with this condition.

The initial condition specifies a Poiseuille inflow for the u -velocity on the left end of the domain, while the initial concentration profile is described by an error function centred around the initial streamwise front location x_0 :

$$c_0 = \frac{1}{2} + \frac{1}{2} \operatorname{erf} \left(\frac{x - x_0}{\delta} \right). \quad (3.1)$$

As the quasisteady tip shape of the two-dimensional displacement front is independent of its initial thickness (Goyal & Meiburg 2006), we set $\delta = 0.1$. A convective outflow boundary condition

$$\frac{\partial \Phi}{\partial t} + U_{\max} \frac{\partial \Phi}{\partial x} = 0 \quad (3.2)$$

is used on ghost nodes at the outflow boundary of the domain, where $\Phi = (u, v, w, c)$, and U_{\max} is the maximum u -velocity within the plane of the outflow boundary.

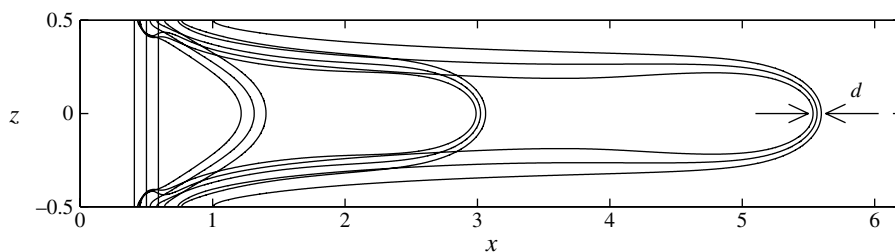


FIGURE 2. Evolution of a quasisteady displacement front for $M = 3$ and $Pe = 1000$. The concentration contours $c = 0.1, 0.5$ and 0.9 are plotted at times $t = 0, 0.5, 1.5$ and 3.0 . The front thickness d is defined as the distance between the $c = 0.1$ and $c = 0.9$ contours along the cell centre ($y = z = 0$).

To avoid potential problems caused by pressure perturbations being reflected off the outflow boundary back into the interior of the domain, inflow and outflow flow rates are computed and global conservation of mass is imposed when the corrector velocities are calculated (Ferziger & Perić 2002). Additional details on the implementation and parallelization algorithms can be found on Oliveira (2012).

3.1. Validation

With the initial conditions specified above, i.e. a Poiseuille inflow for u_i and an error function profile for c , the flow remains effectively two-dimensional in the x, z -plane, since three-dimensional numerical perturbations do not get amplified appreciably over the course of a simulation. Consequently, we can compare the present simulation results with the two-dimensional findings of Goyal & Meiburg (2006) regarding the evolution of the quasisteady displacement front. We remark that the simulations performed by Goyal & Meiburg (2006) solve the Stokes equations, rather than the full Navier–Stokes equations. However, for the present low Reynolds number of $Re = 1$, we expect to find close agreement between the two sets of results.

At the start of the flow, the velocity field immediately deforms the concentration profile near the centre of the cell, while deformations near the walls are mostly due to shear. These changes in the concentration field modify the viscosity field and result in the formation of a well-defined displacement front which propagates along the centre of the cell. The tip of this front reaches a quasisteady configuration, in a moving reference frame, characterized by constant thickness and propagation velocity: see figure 2.

The front thickness d is defined (see figure 2) as the x -distance between the $c = 0.1$ and $c = 0.9$ contours at $z = 0$. It is calculated using cubic spline interpolation of the concentration data. After a transient period, the front thickness reaches a quasisteady value d_0 . We compared our measurements of d_0 for $M = 2$ and $M = 3$ and increasing Pe values against those reported in figure 5 of Goyal & Meiburg (2006), and found that the discrepancy typically lies in the range of 1% to 4%. For the same set of parameters, the dependence of the tip velocity, u_{tip} , on Pe was also investigated. The results from the present Navier–Stokes simulations differ from the Stokes calculations by 0.06–1.2%. This good overall agreement for tip velocity and quasisteady front thickness indicates that the spatial resolution employed in the above calculations is sufficient.

After the base flow is fully developed, we add at time $t = 2$ a small-amplitude perturbation of the most unstable wavelength λ_m , as predicted by the linear stability

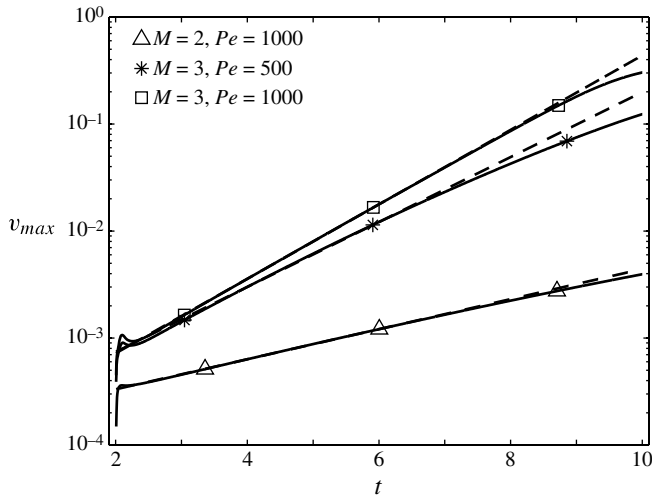


FIGURE 3. Comparison between Navier–Stokes simulations with a small perturbation added to the concentration field, and the linear stability growth rate results of Goyal & Meiburg (2006). The continuous lines show the evolution of the maximum v -velocity for a given set (M, Pe) , while the dashed lines represent the corresponding linear fits.

M	Pe	DNS calculation	Linear growth rate	Error (%)
2	1000	0.323	0.32	1.0
3	500	0.698	0.68	2.7
3	1000	0.792	0.74	7.0

TABLE 1. Comparison between the growth rates obtained by the linear stability analysis based on the Stokes equations of Goyal & Meiburg (2006) and the current direct numerical simulations (see figure 3).

analysis of Goyal & Meiburg (2006). Note that in all of the simulations to be discussed in the following, the spanwise extent of the computational domain was taken equal to the respective value of λ_m . The imposed perturbation shifts the concentration values according to

$$c(x, y, z) \rightarrow c\left(x + A \cos\left(\frac{2\pi}{\lambda_m}y\right), y, z\right), \quad (3.3)$$

where $A = 1 \times 10^{-3}$. We then compare the evolution of the maximum value of the v -velocity with linear growth rate predictions. Results for three sets of parameters are shown in figure 3. The dashed lines represent a linear fit of the data. Table 1 compares the slopes of the linear fit for the DNS calculations with linear growth rate results, showing that the perturbation grows according to the linear prediction for the most amplified wavelength.

4. Quasisteady finger shape

For a constant value of $Re = 1$, we focus on the evolution of the flow for $M = 2, 3, 4$, and 5, and $Pe = 500, 1000, 2000$ and 5000. As mentioned in § 3, the

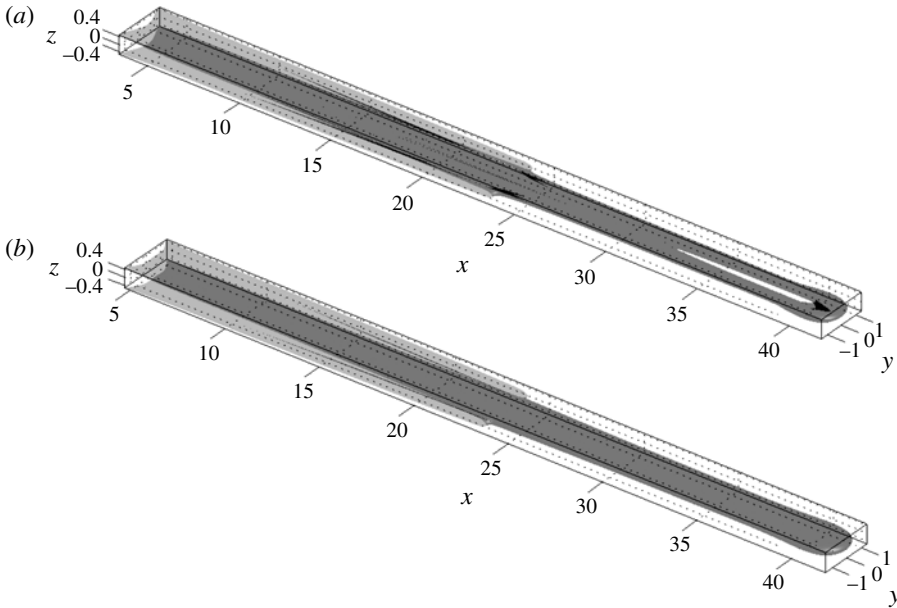


FIGURE 4. Three-dimensional shapes of the $c = 0.3$ (a) and 0.5 (b) concentration isosurfaces for $M = 3$ and $Pe = 1000$ at $t = 22$. In the spanwise direction, the domain extends over one wavelength λ_m , from -1.45 to 1.45 .

initial condition specifies a one-dimensional error-function concentration profile in the streamwise direction, along with a Poiseuille flow velocity field. The effectively two-dimensional simulations described in § 3 showed that this velocity field immediately deforms the concentration distribution in the interior of the gap. After the flow reaches a quasisteady state in the tip region around $t = 2$, we add one wavelength of a wavy displacement to the concentration field, with the wavenumber of the linearly most unstable mode and an amplitude of 0.1. The domain extends from $-\lambda_m/2$ to $\lambda_m/2$ in the spanwise direction, and the phase of the concentration displacement is chosen such that the front is most advanced at the spanwise centre of the computational domain, i.e. at $y = 0$. From this time on, the simulations become fully three-dimensional. Figure 4 shows perspective views of the concentration isosurfaces $c = 0.3$ and 0.5 for $M = 3$ and $Pe = 1000$ at $t = 22$, when the tip velocity and shape are quasisteady. The $c = 0.5$ contour displays a long, smooth finger, similar to corresponding observations for immiscible displacements by other authors: see Homsy (1987) and references therein. The features of the $c = 0.3$ isosurface, and specifically the hole that has opened up behind the finger tip, will be discussed below.

As we did for the earlier, two-dimensional simulations, we define the finger tip position x_{tip} as the location where $c = 0.5$ along $y = z = 0$. Figure 5(a) indicates that for all parameter combinations investigated here, the tip advances at a nearly constant rate for an extended time interval. Figure 5(b) displays the dependence of this quasisteady tip velocity $u_{tip} = dx_{tip}/dt$ on Pe and M . We find that the tip velocity generally increases for larger viscosity contrasts and lower diffusivities. Figure 5(b) also compares the quasisteady tip velocities of the three-dimensional fingers with the corresponding front velocities of the two-dimensional base flows. The dependence of the front velocity on Pe and M is seen to be more pronounced for three-dimensional

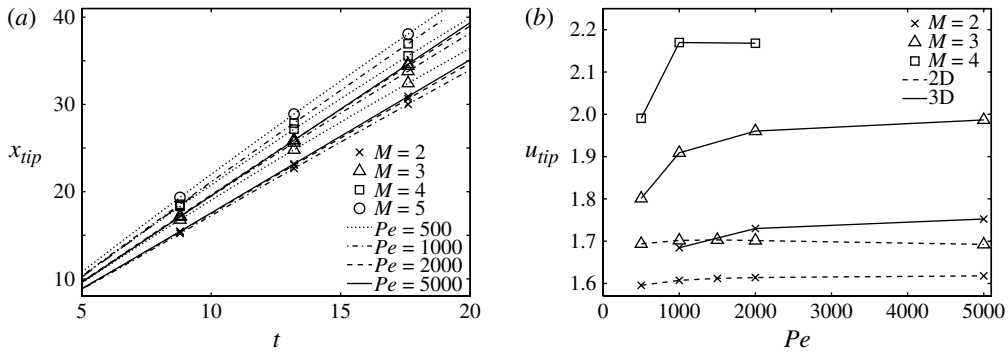


FIGURE 5. (a) Finger tip location x_{tip} as function of time, for various Péclet numbers and viscosity contrasts. For all parameter combinations investigated, the finger tip advances with a nearly steady velocity over an extended time interval. (b) Quasisteady tip velocity u_{tip} as function of Pe for different M . The continuous curves show the tip velocities of three-dimensional (3D) fingers, while the dashed lines represent the corresponding results for the two-dimensional (2D) base states. Generally, the tip advances faster for larger viscosity contrasts and for larger Péclet numbers in both situations. However, the influence of M is more pronounced for three-dimensional flows than for the two-dimensional base states.

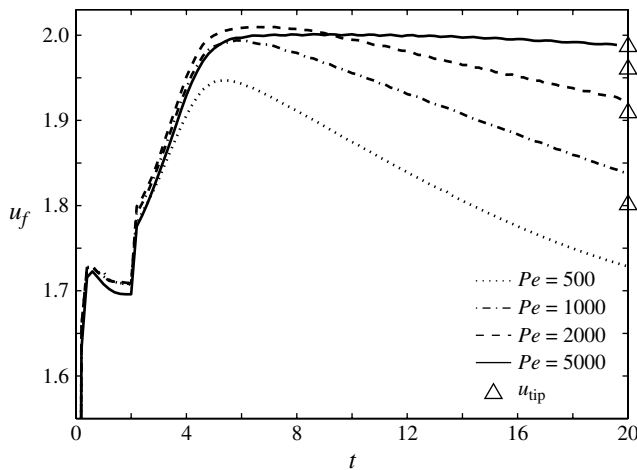


FIGURE 6. The fluid velocity u_f at the finger tip location. After an initial period of growth, u_f decreases and drops below the quasisteady tip velocity (indicated by the triangles on the right vertical axis). For increasing Pe , the difference between u_f and u_{tip} is seen to diminish.

displacements. This reflects the fact that the mobility ratio has a strong effect on the effective width of the finger, and on the layer of resident fluid left behind on the walls of the Hele-Shaw cell.

Figure 6 displays the u -velocity u_f of the fluid at the tip location x_{tip} as function of time, for various combinations of the governing parameters. For comparison, the quasisteady tip velocity u_{tip} is also shown. We find that, after an initial transient period of growth, the fluid velocity u_f at the tip decays with time and drops below the tip velocity u_{tip} . In other words, the $c = 0.5$ concentration contour advances faster than the fluid particle at its location. Hence, elements of the resident fluid continuously cross

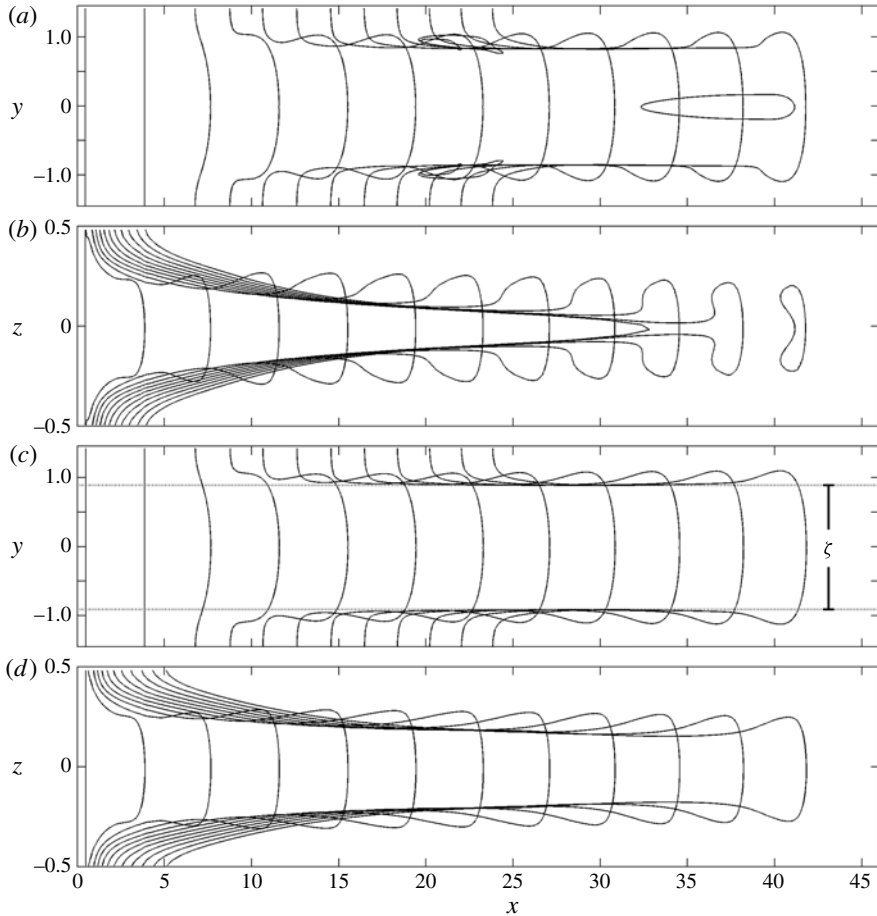


FIGURE 7. Two-dimensional concentration contours $c = 0.3$ (*a, b*), and 0.5 (*c, d*) in the two central symmetry planes, $z = 0$ and $y = 0$, respectively. $(Pe, M) = (1000, 3)$ and the times shown are $t = 0, 2, \dots, 22$. The closed loop emerging behind the finger tip in (*a*) and the corresponding pinch-off shown in (*b*) are related to the hole visible in the perspective view of the $c = 0.3$ contour in figure 4(*a*). (*c*) The intersecting $c = 0.5$ contours in the $z = 0$ plane define straight lines, which indicate that the finger achieves a quasisteady width ζ . On the other hand, (*d*) demonstrates that the finger does not have a constant thickness in the cross-gap direction.

the boundary of the finger (defined by the $c = 0.5$ contour) at the tip from outside the finger to the inside, while their concentration changes from $c > 0.5$ to $c < 0.5$. We will return to this point below when discussing the corresponding streamline patterns. As we increase Pe , thus reducing diffusive effects, u_f approaches the quasisteady value of u_{tip} , so that the flux of fluid elements across the $c = 0.5$ contour is diminished.

Figure 7 displays the $c = 0.3$ and 0.5 concentration contours along the two central symmetry planes $z = 0$ and $y = 0$, respectively, for $(Pe, M) = (1000, 3)$ at times $t = 0, 2, \dots, 22$. The intersecting $c = 0.5$ contours in the $z = 0$ plane (see figure 7*c*) define straight lines which indicate that the finger achieves a quasisteady width ζ . On the other hand, figure 7(*d*) demonstrates that the finger does not have a constant thickness in the cross-gap direction. Hence, the film of displaced fluid left behind on the wall

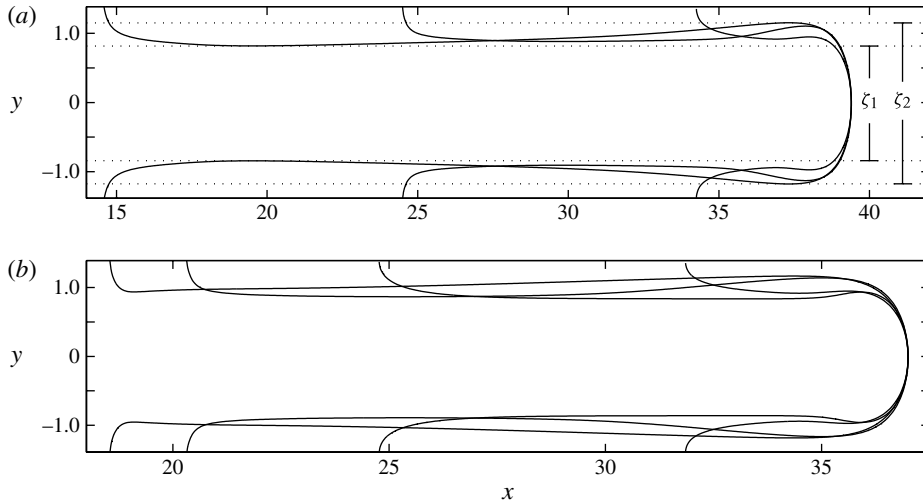


FIGURE 8. Concentration contours $c = 0.5$ at time $t = 18.8$ within the centre plane $z = 0$ for (a) $Pe = 1000$ and increasing viscosity ratios $M = 2, 3$ and 4 , and (b) $M = 3$ and increasing Péclet numbers $Pe = 500, 1000, 2000$ and 5000 . Larger viscosity contrasts and lower diffusion result in longer fingers with wider tips. Note that the contours have been shifted so that the finger tips are in identical locations. ζ_1 (ζ_2) indicates the minimum (maximum) finger width of $(M, Pe) = (4, 1000)$.

of the Hele-Shaw cell does not have a constant thickness either. The closed loop emerging behind the finger tip in the $c = 0.3$ contour of figure 7(a), along with the corresponding pinch-off shown in figure 7(b), are related to the hole visible in the perspective view of the $c = 0.3$ contour in figure 4(a). These features will be discussed in detail below.

Figure 7 suggests that the width of the finger can be suitably characterized by a single parameter m , defined by

$$m = \frac{\zeta}{\lambda_m}, \quad (4.1)$$

where ζ is evaluated by means of the $c = 0.5$ contour within the centre plane $z = 0$. However, simulations for other values of M and Pe show that for most fingers the width varies significantly in the streamwise direction. The influence of the viscosity ratio on the finger shape can be assessed in figure 8(a). Here, the Péclet number is kept fixed at $Pe = 1000$, and $c = 0.5$ contours for $M = 2, 3$ and 4 are superimposed. Similarly, figure 8(b) displays $c = 0.5$ contours for $M = 3$ and increasing Péclet numbers. Larger viscosity contrasts and lower diffusivities are seen to result in longer fingers with wider tips. In light of the above observations, we employ both the minimum width $m_1 = \zeta_1/\lambda_m$ and the maximum width $m_2 = \zeta_2/\lambda_m$ in order to characterize the finger shape.

Figure 9(a) shows the variation of m_1 and m_2 with time for $Pe = 1000$ and $M = 2, 3$ and 4 . Note that for larger viscosity contrasts, minimum and maximum widths emerge earlier in time, indicating that the finger width becomes non-monotonic more rapidly. Subsequently, the difference between m_1 and m_2 increases with time for all simulations, and most quickly for large values of M . Only for $(M, Pe) = (3, 1000)$ does m_1 reach a steady state. Figure 9(b) shows the influence of Pe on m_1 and m_2

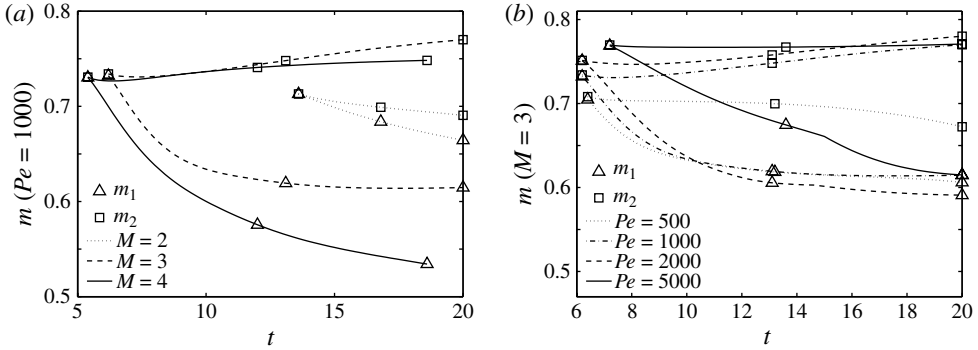


FIGURE 9. (a) The time-dependent width parameters for $Pe = 1000$ and increasing viscosity ratios. For larger values of M , minimum and maximum width values form earlier in time. The difference between m_1 and m_2 subsequently grows with time, most rapidly for large viscosity contrasts. (b) The time-dependent width parameters for $M = 3$ and increasing values of Pe . Larger Péclet numbers are seen to result in wider fingers. The finger width parameters depend much more weakly on the Péclet number than on the viscosity contrast.

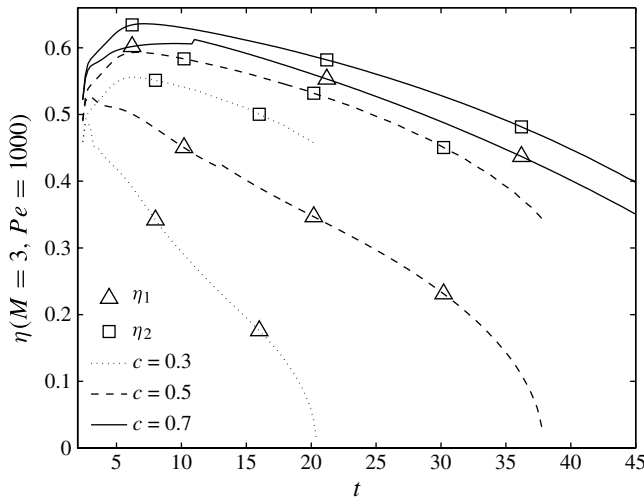


FIGURE 10. Minimum and maximum film thicknesses along the centre of the finger for $(M, Pe) = (3, 1000)$ and $c = 0.3, 0.5,$ and 0.7 .

for $M = 3$. Lower diffusivities generally lead to wider fingers. The emergence of a minimum and maximum width is seen to depend much more weakly on the Péclet number than on the viscosity contrast.

In complete analogy to the above finger width parameters in the spanwise direction, we can define η_1 (η_2) as the minimum (maximum) finger thickness in the z -direction within the $y = 0$ plane. Figure 10 shows the evolution of η_1 and η_2 for $c = 0.3, 0.5$ and 0.7 . All thickness values decrease in time, indicating that the c -contours move from the top and bottom walls toward the centre plane. The pinch-off seen in figure 7(b) is clearly visible in figure 10 around $t = 20$.

Based on the above analysis of the concentration field in the spanwise and cross-gap directions, we can now proceed towards a discussion of the one-

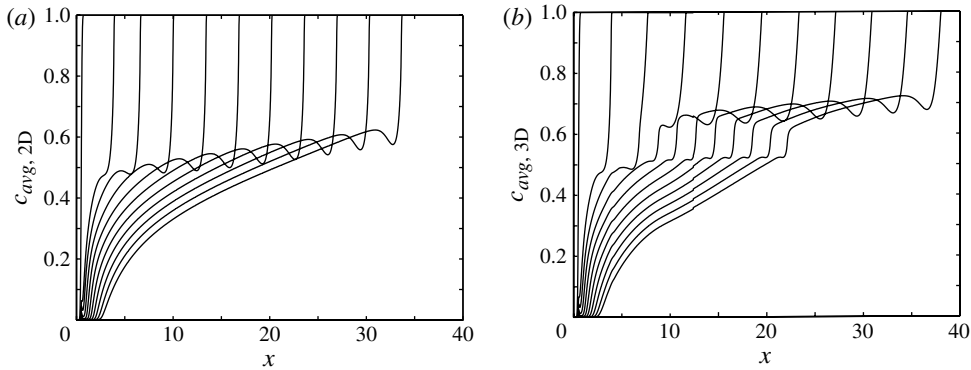


FIGURE 11. Cross-section-averaged concentration profiles for $(M, Pe) = (3, 1000)$ at times $t = 0, 2, \dots, 20$ comparing (a) the evolution of the base state with (b) full three-dimensional simulations displaying instability growth. The instability grows after a perturbation is introduced at $t = 2$. The plateau near $c_{avg,3D} = 0.5$ and the subsequent steep concentration gradient indicate the location of the root of the finger and its shoulders.

dimensional $c_{avg}(x)$ -profiles obtained by averaging across the entire y, z -cross-section. For $(M, Pe) = (3, 1000)$, figure 11 compares such cross-sectional averages for the two-dimensional, unperturbed base flow and the three-dimensional finger case. The times $t = 0, 2, \dots, 20$ are shown. The first two profiles are identical in both cases, the first one being the imposed error function at $t = 0$. For the two-dimensional case shown in figure 11(a), the existence of minimum (η_1) and maximum (η_2) thickness values discussed earlier is reflected in the streamwise non-monotonicity of c_{avg} . In figure 11(b), the spanwise instability begins to grow after the perturbation is imposed at $t = 2$. Subsequently, the concentration profile advances more rapidly than for the two-dimensional base case. The spanwise instability further results in the formation of a ‘shoulder’ or plateau in the profile with $c_{avg} \approx 0.5$. This shoulder extends to the root of the finger, i.e. to the valley that connects two neighbouring fingers. Since the emerging finger occupies only a fraction of the spanwise domain width, the c_{avg} -values are larger in the region of the finger, and typically lie in the range 0.6–0.7. The existence of minimum and maximum width and thickness values for the finger, discussed earlier, result in the streamwise non-monotonicity of the averaged concentration profiles.

Figure 12 shows the gap-averaged concentration field for $(Pe, M) = (1000, 3)$ at $t = 20$. Here, darker regions correspond to less viscous fluid, and the contour lines represent $c = 0.1, 0.2, \dots, 0.9$. Different contour levels have very different shapes. Small concentration values ($0.3 < c < 0.5$) display two-fingered patterns, while large concentration values ($0.7 < c < 0.9$) exhibit single finger structures with contour lines placed closer together. The $c = 0.6$ contour represents the transition between these two regimes, as it shows a ‘hole’ some distance behind the front.

Figure 13 shows the temporal evolution of the three gap-averaged concentration contours (a) $c = 0.5$, (b) $c = 0.6$, and (c) $c = 0.7$, for the same set of parameters as figure 12. Successive contours correspond to times $t = 0, 2, \dots, 20$. Figure 13(a) indicates that the $c = 0.5$ contour evolves in a very complex fashion. A ‘hole’ opens up some distance behind the front and subsequently grows in time. It catches up with the front and has almost reached it by $t = 12$ (indicated by lighter, grey contours). At $t = 14$, it has reached the front and caused it to split into two elongated fingers,

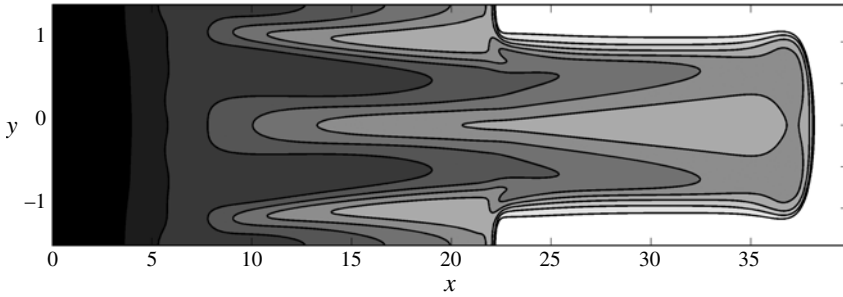


FIGURE 12. Gap-averaged concentration field for $M = 3$, $Pe = 1000$ at $t = 20$. Darker regions are associated with smaller viscosities. The contour lines correspond to the values $c = 0.1, 0.2, \dots, 0.9$.

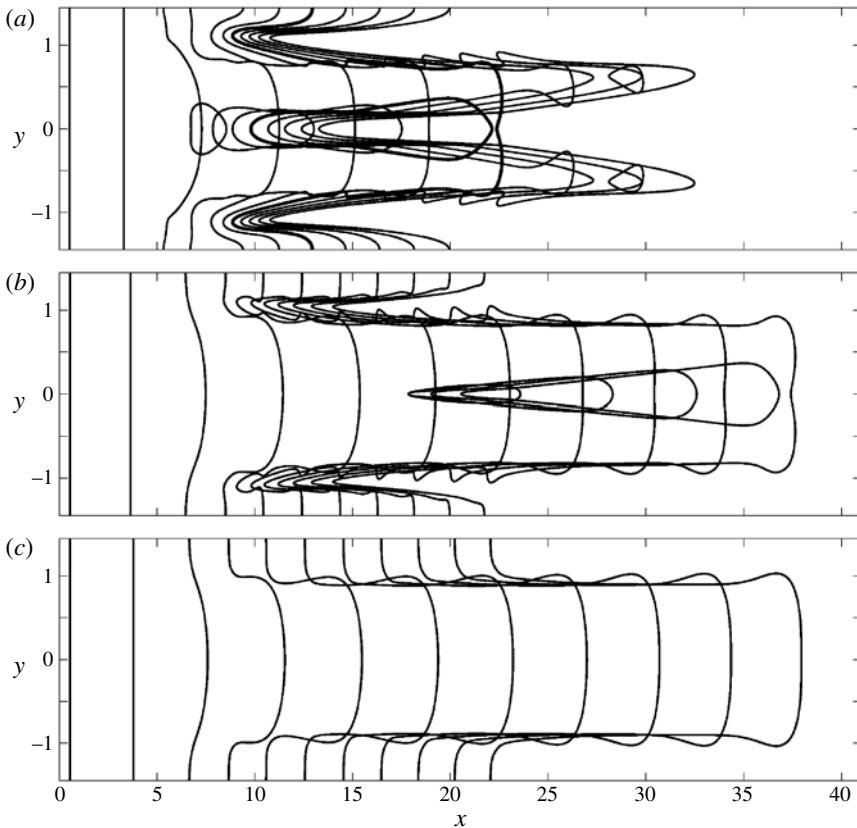


FIGURE 13. Gap-averaged profiles for $M = 3$, $Pe = 1000$ at $t = 0, 2, \dots, 20$ for concentration levels (a) $c = 0.5$, (b) $c = 0.6$ and (c) $c = 0.7$.

an event that we term ‘inner splitting’, in contrast to the tip-splitting described by Tan & Homsy (1988) for miscible flows. A short time later, at $t = 16$, two ‘droplets’ have detached from the tips of these fingers. For $t = 18$ and 20 , we observe two fingers with sharp tips. Also, note the deep indentations on the sides of these two central fingers near $|y| = 1$, which effectively give rise to the existence of a third, shorter finger along

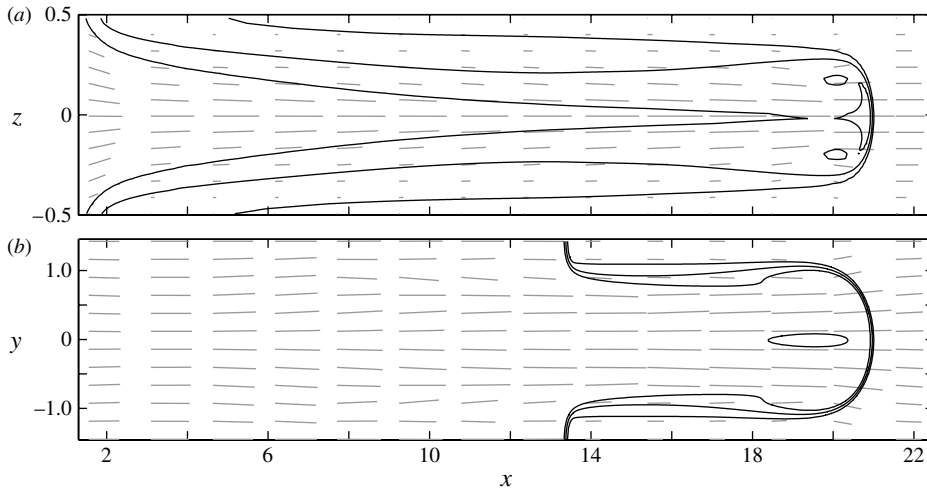


FIGURE 14. Concentration contours (dark) and velocity vectors in the laboratory reference frame (light) in the $y = 0$ (a) and $z = 0$ (b) symmetry planes at $t = 10.8$. The concentration levels correspond to $c = 0.1, 0.5$ and 0.9 . Resident fluid is being convected from the walls towards the centre of the gap, while the injected fluid moves laterally away from the centre of the finger.

the spanwise boundary of the Hele-Shaw cell. Section 5 will address the mechanisms behind the formation of these features.

The $c = 0.6$ contour, shown in figure 13(b), follows a similar evolution, albeit more slowly. The ‘hole’ behind the front does not form until $t = 14$, and by $t = 20$ it has not quite caught up with the front. In contrast, the $c = 0.7$ gap-averaged contour, depicted in figure 13(c), is still fully intact at $t = 20$. A hole has not yet formed, and there is no indication of the deep indentations on the sides of the central finger that we had seen for $c = 0.5$ and 0.6 .

5. Inner splitting mechanism

We now address the mechanism responsible for the inner splitting phenomenon described above. Towards this end, we focus on the displacement with $M = 3$ and $Pe = 1000$ shown in figure 4, which had served as the basis for much of the above discussion. Specifically, we will demonstrate the important role played by the cross-gap velocity and the streamwise vorticity, neither one of which can be captured by a gap-averaged Darcy approach.

Figure 14 shows the concentration contours in the $y = 0$ (a) and $z = 0$ (b) symmetry planes at time $t = 10.8$. Figure 14(a) indicates that along the entire length of the finger, the cross-gap velocity in the $y = 0$ symmetry plane is directed from the walls towards the centreline, thereby transporting the resident fluid towards the centre of the gap. This inflow of resident fluid from the walls, when combined with the effects of diffusion, causes the pinch-off of the $c = 0.1$ contour visible in the figure. Similarly, figure 14(b) demonstrates that within the $z = 0$ symmetry plane, over much of the length of the finger the injected fluid is transported laterally away from the centreline of the finger.

Further insight can be gained by analysing the flow field within $x = \text{const.}$ cross-cuts at various streamwise locations. Figure 15 shows concentration contours along with the

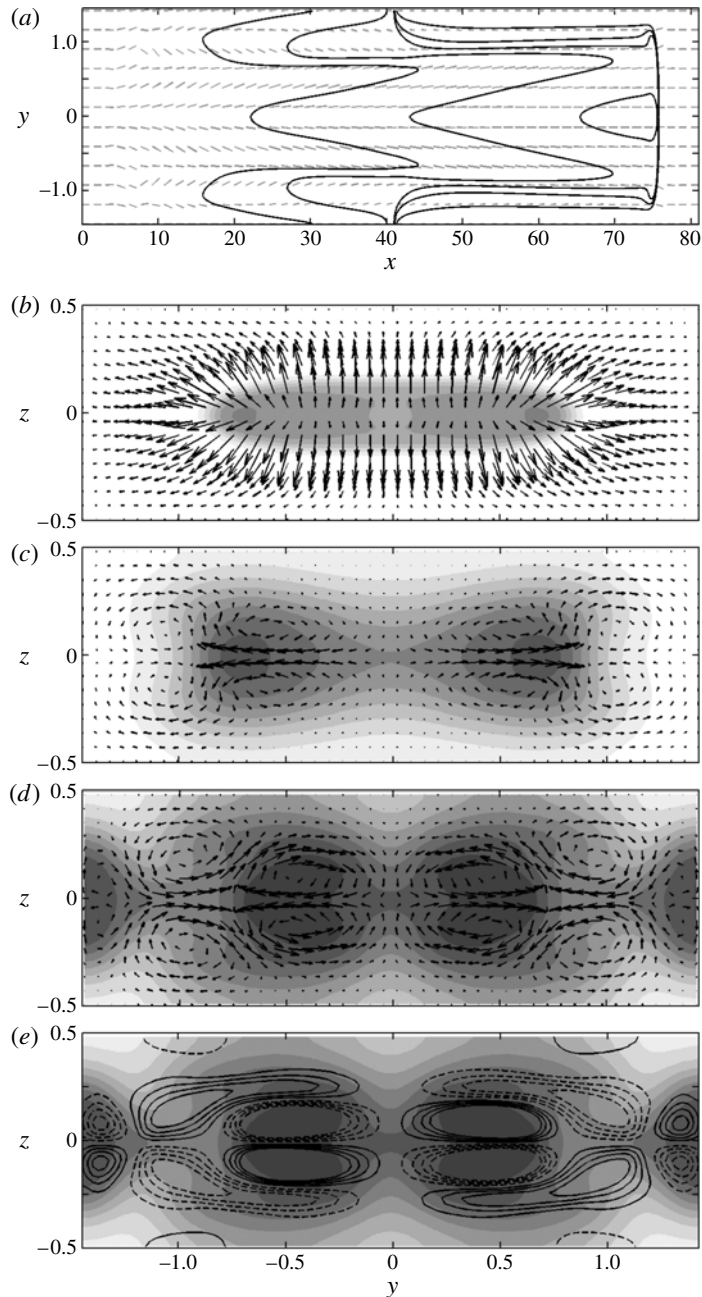


FIGURE 15. (a) Concentration contours (black) and velocity vectors (grey) in the plane $z = 0$ for $M = 3$ and $Pe = 1000$ at time 42. (b–d) show cross-sections at $x = 75.5$, 54 and 30, respectively. In these cross-sections, the black arrows show the direction of the velocity field in the y, z -plane, while the grey shading represents the concentration field. Some distance behind the tip, we recognize the existence of a streamwise vorticity quadrupole that convects resident fluid from the walls to the cell centre near $y = 0$, and injected fluid laterally away from the cell centre near $z = 0$. This streamwise vorticity quadrupole causes the finger to split longitudinally. (e) Streamwise vorticity contours (black lines) and c -contours (grey shading) at $x = 30$. Continuous (dashed) contour lines represent positive (negative) vorticity values.

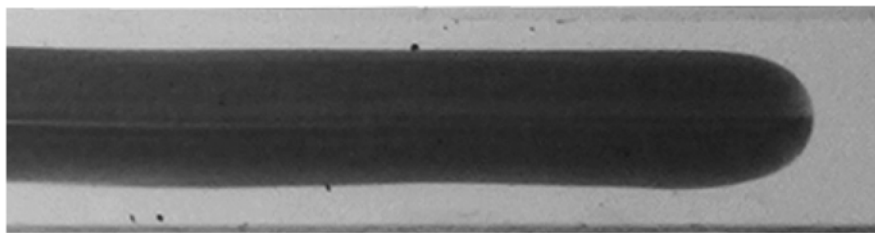


FIGURE 16. Experimental evidence of inner splitting instability can be found in preliminary experiments by Tony Maxworthy (personal communication) designed in order to visualize this phenomenon. Here, a lighter band of displaced fluid bisects the centre of the dark, less viscous finger along the centreline.

v - and w -velocity components for cross-sections near the tip (b), through the finger (c), and upstream of the shoulder (d). We recognize that near the tip the displaced fluid is being pushed away in all directions. Some distance behind the tip, a quadrupole structure of streamwise vorticity emerges that transports resident fluid from the wall to the centre of the gap near $y = 0$, while injected fluid is transported laterally away from the finger's centre along $z = 0$. This is consistent with the longitudinal cross-cuts shown in figure 14, and it explains the pinch-off of the concentration contours along the centreline of the flow. Further back along the finger, upstream of the shoulder region, additional secondary streamwise vortices exist that transport resident fluid towards the centreline near $y = \pm 1$, thereby leading to the strong indentations visible in figure 13(a,b).

We note that the tendency of the v -velocity to widen the front laterally can already be observed during the linear stages: see the eigenfunctions shown by Goyal & Meiburg (2006) in their figure 13. In a reference frame moving with the front, those authors show that the growth of the instability gives rise to counter-rotating vortices in the x, y -plane, which accelerate and widen the front.

5.1. Experimental evidence

Figure 16 shows preliminary experimental results by Tony Maxworthy (personal communication) on the problem under consideration. It shows a long diffusive dark finger displacing the resident more viscous fluid. Along the centre of the finger, the lighter band bisecting the finger is an indication of the inner splitting mechanism.

We remark that a similar phenomenon of longitudinal finger splitting was observed by Petitjeans & Maxworthy (1996) (see figure 17) in a miscible horizontal displacement of glycerine by a glycerine–water mixture in a capillary tube. Those authors suggested that this splitting might be driven by gravity, and represent a miscible version of the classical Rayleigh–Taylor instability. Corresponding axisymmetric Stokes simulations in the companion paper by Chen & Meiburg (1996) showed good overall agreement with the experimental observations of Petitjeans & Maxworthy (1996), both regarding the finger width and the formation of a protrusion at the finger tip. However, two-dimensional simulations within a transverse cross-section were unable to reproduce the experimentally observed longitudinal splitting phenomenon. Vanaparthi & Meiburg (2008) went one step further and performed three-dimensional Stokes simulations that included gravitational forces. Still, these simulations did not reproduce the longitudinal finger-splitting phenomenon observed by Petitjeans & Maxworthy (1996). Based on the findings of the present investigation, we hypothesize that the longitudinal splitting observed by Petitjeans & Maxworthy

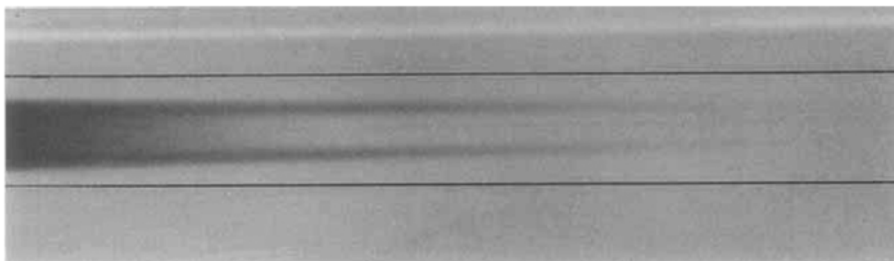


FIGURE 17. The longitudinal finger-splitting phenomenon observed by Petitjeans & Maxworthy (1996) in miscible displacements in capillary tubes shows features similar to the inner splitting discussed here, e.g. figure 13(a).

(1996) may be due to a mechanism similar to the one described here, and unrelated to gravitational forces. The simulations by Vanapathy & Meiburg (2008) most likely did not reproduce this phenomenon because they were not run for a sufficiently long time.

Further experimental evidence for longitudinal finger splitting can be found in the miscible Hele-Shaw experiments of Wooding (1969). The figures in plates 1 and 3 (plate 3 is reproduced in figure 18) of his paper show very elongated, upward-propagating light-coloured finger structures, some of which are longitudinally bisected by narrow dark regions. We have to keep in mind, however, that the flows investigated by Wooding (1969) were gravitationally driven, with negligible viscosity differences between the fluids. It will hence be interesting to extend the current investigation to miscible fluids of different densities, in order to evaluate the importance of inner splitting in such flows.

5.2. Influence of the Péclet number

To assess the influence of the Péclet number on the inner splitting mechanism, we conducted a simulation for $(M, Pe) = (3, 500)$. Again, the spanwise width of the computational domain was taken to be equal to the linearly most unstable wavelength. Upon perturbing the flow at $t = 2$, a finger forms and subsequently develops an inner splitting, as seen before for $Pe = 1000$: see figure 19 at $t = 22$. However, diffusion is sufficiently strong for the fingers to subsequently merge again, as can be seen from the $c = 0.5$ contour at $t = 70$. We conclude that the role of the Péclet number in the evolution of the inner splitting is subtle. A certain amount of diffusion is required for the splitting to develop, but too much diffusion can overwhelm the convective transport that causes the fingers to separate. Hence, for very large Pe , it may take very long for the splitting to appear, while in flows with Péclet numbers that are too low, the tendency towards splitting may not be strong enough to overcome the effects of diffusion.

6. Vorticity dynamics

We now focus on the mechanisms behind the generation of streamwise vorticity, and specifically on the formation of the quadrupole structure. For inviscid or nearly inviscid flows, such mechanisms can frequently be analysed in a straightforward fashion, based on the tilting and stretching terms in the streamwise vorticity equation, and the fact that vortex tubes maintain their identity. For the present case of very low Reynolds numbers, on the other hand, the interpretation of the physical processes governing the formation of streamwise vorticity becomes more difficult, as

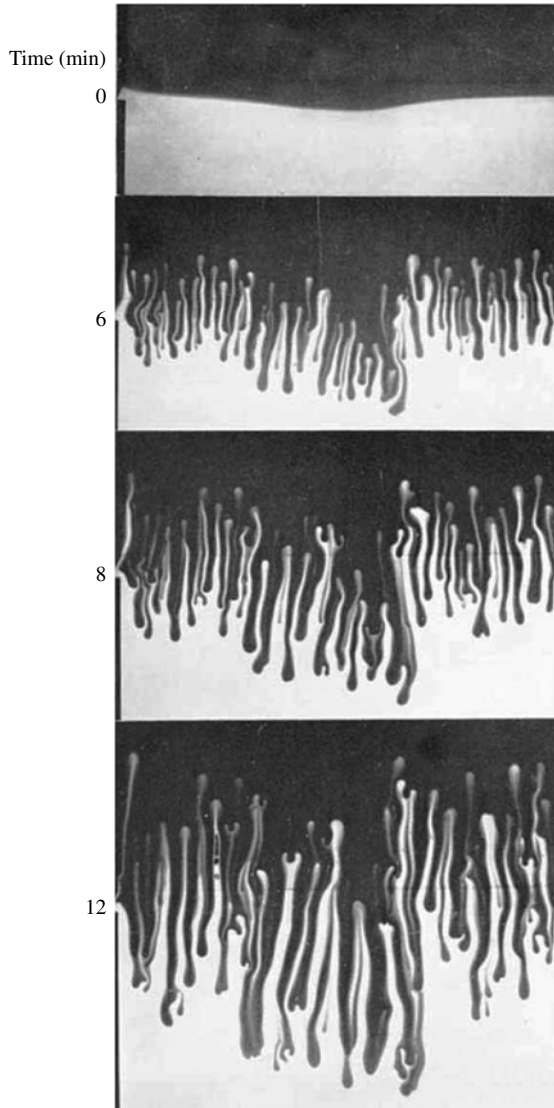


FIGURE 18. Evidence of inner splitting in the gravity-driven, miscible instability experiments by Wooding (1969). Some of the very elongated, upward-propagating light finger structures are longitudinally bisected by narrow dark regions.

the vorticity equation is dominated by the viscous terms. Furthermore, vortex lines are subject to viscous reconnection, so that they lose their identity. Nevertheless, a vorticity-based analysis of the flow can provide considerable insight into the governing mechanisms.

Far upstream of the finger, where the flow is of plane Poiseuille type, only spanwise vorticity exists. This vorticity has the form of two plane layers of opposite signs, whose strength decays from a maximum at the wall to zero at the centreline. For $z > 0$ ($z < 0$), this spanwise vorticity points in the $-y$ -direction ($+y$ -direction). As these two vorticity layers are convected towards the root of the finger, they undergo a deformation. In the central section near $y = 0$ the fluid accelerates as it

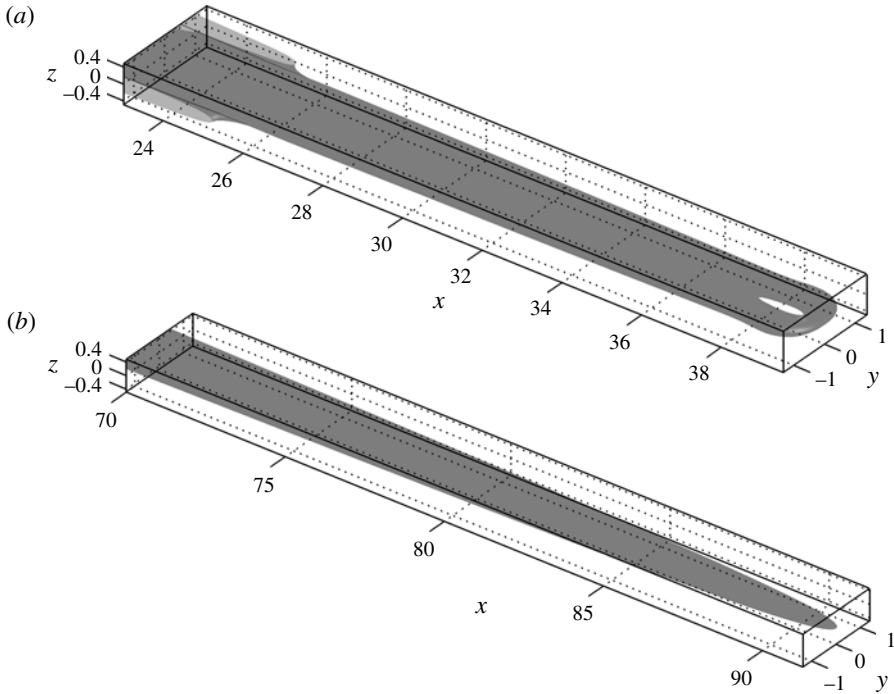


FIGURE 19. Three-dimensional profile of the $c = 0.5$ concentration isosurface for $M = 3$, $Re = 1$ and $Pe = 500$ at times $t = 22$ (a) and 70 (b). Diffusion is sufficiently strong for the fingers to merge again, after having split earlier.

enters the finger, while the flow velocity is reduced near the finger's shoulders at the spanwise boundaries. Hence, inviscid arguments suggest that the initially purely spanwise vorticity is tilted into the streamwise direction in the following fashion: the negative spanwise vorticity within the region $z > 0$ will be tilted so that it points in the $+x$ -direction for $y > 0$, and in the $-x$ -direction for $y < 0$. The initially positive spanwise vorticity in the region $z < 0$ acquires the opposite streamwise direction, i.e. it will point in the $-x$ -direction for $y > 0$, and in the $+x$ -direction for $y < 0$. This tilting of the initially spanwise vorticity into the streamwise direction in the vicinity of the finger's root represents the main mechanism responsible for the formation of the quadrupole structure of the streamwise vorticity. This strongly elongated quadrupole is clearly visible in figure 20, in the region $6 < x < 25$.

However, as the figure shows, this tilting mechanism does not exist in isolation, and a more compact quadrupole structure of the opposite sign exists right at the finger's shoulders. This quadrupole owes its existence to a fundamentally different mechanism, as will be explained now. As the injected fluid approaches the root of the finger from upstream and slows down near the spanwise boundaries, it acquires a small spanwise velocity component that drives it from the spanwise boundaries towards the central region near $y = 0$, where it subsequently enters the finger. This can be clearly seen, for example, in figure 21. As a result of this fluid flow from the spanwise boundaries towards the central $y = 0$ region, the two Poiseuille flow layers of spanwise vorticity move from the walls towards the $z = 0$ plane near the spanwise boundaries, while they are pushed towards the walls at $y = 0$. This results in the vortex line configurations shown in figures 22 and 23. We recognize that already near $x = 2$ opposite-signed

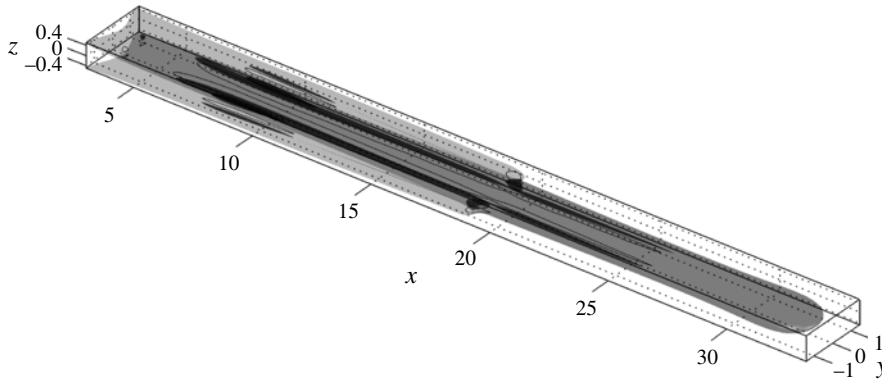


FIGURE 20. Perspective view of the $c = 0.5$ concentration isosurface (light grey), along with the $|\Omega_x = 1|$ contours. Positive (negative) streamwise vorticity is shown in dark grey (transparent) at time $t = 17$ for $(M, Pe) = (3, 1000)$.

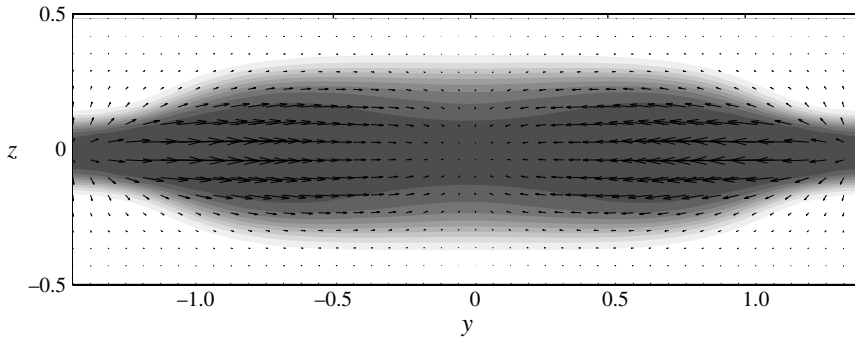


FIGURE 21. Crosscut at $x = 8.7$ and $t = 6$ for the flow shown in figure 22. The grey shading depicts the concentration field, while the arrows show the (v, w) -velocity field carrying fluid from the spanwise boundaries towards the centre.

vortex lines from the two Poiseuille layers approach each other near the spanwise boundaries. Near $x = 8.15$, these vortex lines are seen to reconnect near $y = \pm 1.1$, thereby forming closed vortex loops that extend from $y = 1$ to $y = -1$. There are two inviscid mechanisms that can potentially contribute to the acceleration of the fluid in the regions of viscous reconnection near $y = \pm 1$. First of all, as mentioned above, the two opposite-signed Poiseuille flow vorticity layers approach each other in this region, thereby inducing a larger streamwise velocity upon each other. Secondly, the newly formed closed vortex loops possess strong curvature in the reconnection region, which should also contribute to their streamwise acceleration. The overall effect is that near $x = 8.15$ the sections of the vortex lines near $y = 0$ trail behind the sections closer to the finger's shoulder, as can be seen clearly in the top view of figure 22. Consequently, the streamwise vorticity in this region is opposite in sign to that of the elongated quadrupole.

The viscous vortex reconnection process described above results in the formation of a gap-wise vorticity component pointing in the z -direction. It is this z -vorticity component that drives the viscous fingering instability in the classical gap-averaged, Darcy sense. As seen in figure 24, it forms elongated layers along the sides of the

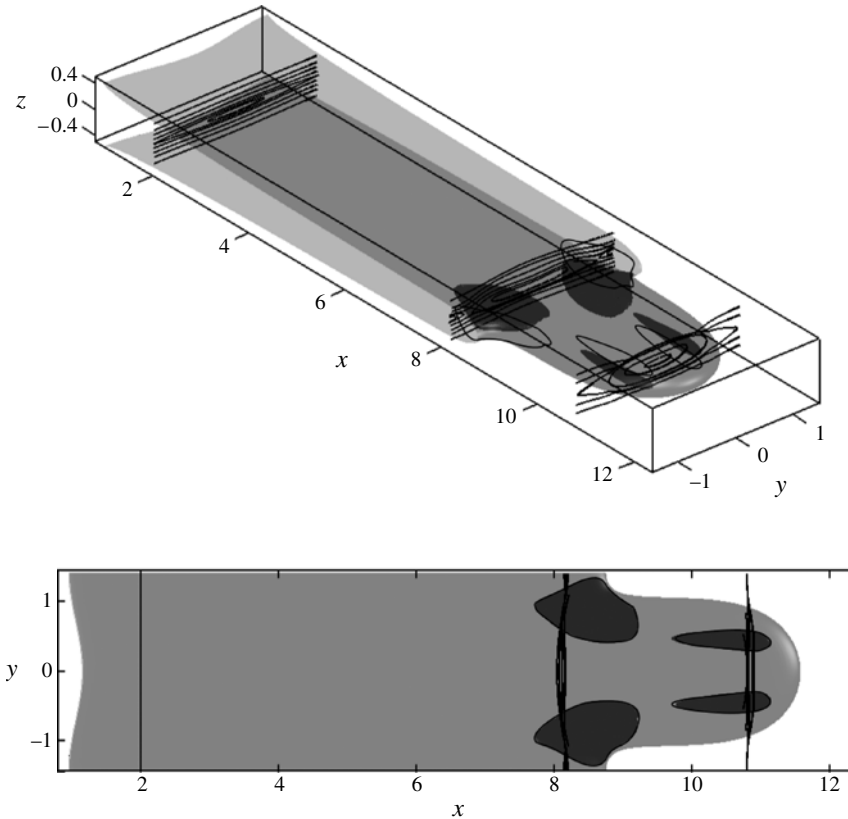


FIGURE 22. Perspective and top view of finger at time $t = 6$ showing the $c = 0.5$ concentration isosurface in light grey, and the $|\Omega_x| = 1.2$ contours in dark grey (positive) and transparent (negative). In addition, vortex lines near $x = 2, 8.15$, and 10.8 are also shown.

finger. These layers accelerate the fluid within the finger, while slowing down the fluid near the spanwise boundaries.

As the high-speed fluid within the central finger is surrounded by low-speed fluid both at the walls and near the spanwise boundaries, we expect the fluid within the finger to be encapsulated by closed vortex loops. This is confirmed by the perspective and top views of the vortex lines near $x = 10.8$ in figure 22, as well as by the corresponding streamwise view in figure 23. These views show that in the finger region the vorticity field is primarily aligned in the azimuthal y - and z -directions, while the streamwise x -component that gives rise to the quadrupole structure is comparatively weak.

7. Comparison with immiscible fingering

We now discuss a few of the similarities and differences, respectively, between miscible and immiscible displacements, along with the roles of the Péclet and capillary numbers in these flows. Of particular interest is the question as to whether increasing Pe -values influence miscible displacements in the same way as increasing capillary numbers affect immiscible displacements.

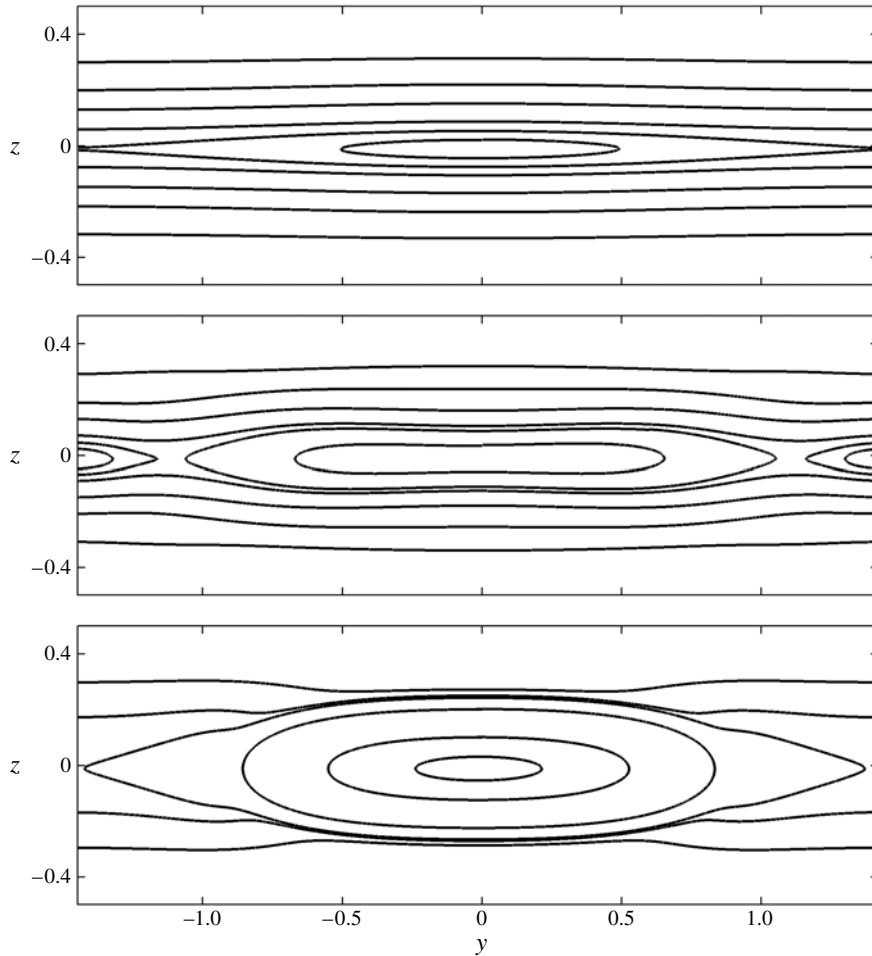


FIGURE 23. Streamwise view of the vortex lines plotted in figure 22. From top to bottom, these lines are located near $x = 2, 8.15,$ and 10.8 .

McLean & Saffman (1981) employ Darcy's law to calculate the dimensionless finger width $m = w/D$ as a function of the capillary number $Ca = \mu U/T$. Here w denotes the dimensional finger width, while D represents the width of the Hele-Shaw apparatus. μ indicates the viscosity of the driven fluid, U the tip velocity of the finger, and T the interfacial tension. In their calculation, the authors assume that the viscosity ratio is infinite, and that the resident fluid is completely expelled from the gap by the advancing finger. Their results show qualitative agreement with the experimental results of Pitts (1980) and Saffman & Taylor (1958). The incorporation of a constant film thickness η left behind on the walls of the cell improves the quantitative agreement only slightly, and the authors suggest that $\eta \neq \text{const.}$ may have to be considered to obtain further improved agreement.

Both experiments and analysis show a tendency for immiscible fingers to propagate faster for larger Ca . The present investigation shows a corresponding trend for larger Pe : see figure 5(b). Regarding the finger width, the comparison is not as straightforward. Immiscible Hele-Shaw experiments at moderate capillary numbers typically show a finger width that is nearly constant along the length of the finger.

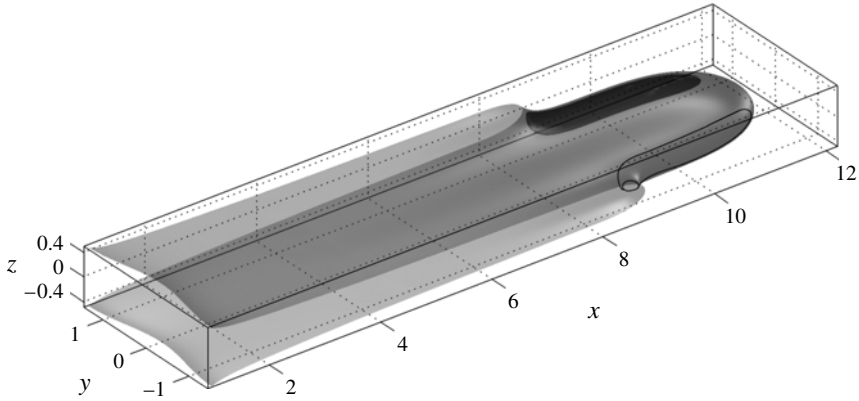


FIGURE 24. Perspective view at time $t = 6$ showing the $c = 0.5$ concentration isosurface in light grey, along with the $|\Omega_z| = 3.5$ contours. The dark grey surface represents the positive value, while the transparent plots the negative one.

t	M	Pe	m_2
20	3	500	0.6719
20	3	1000	0.7699
20	3	2000	0.7797
20	3	5000	0.7708
10	4	500	0.7344
10	4	1000	0.7365
10	4	2000	0.7489
10	4	5000	0.7526

TABLE 2. Maximum width of the $c = 0.5$ contour across the cell centre at $t = 20$ for $M = 3, 4$ and $Pe = 500, 1000, 2000$, and 5000 .

In contrast, the present simulations indicate that for miscible flows, the finger width varies in the streamwise direction. While the finger width reaches a maximum value m_2 near the head, it becomes increasingly narrow towards its root, as a result of lateral diffusion. Nevertheless, table 2 shows a tendency towards larger values of m_2 , i.e. wider fingers, for larger Pe . This is in contrast to observations for immiscible flows, which show narrower fingers for increasing Ca . Hence, while smaller surface tension results in narrower fingers, lower diffusivity produces wider fingers, as it prevents the diffusion of displaced fluid into the finger. In this context we note that there are, of course, other equally justifiable ways to define the finger width, e.g. via integral measures. Such alternative diagnostics have not been explored within the current investigation.

We never saw fingers emerge with $m_2 < 0.5$, which is consistent with immiscible observations (with the exception of the findings by Kopf-Sill & Homsy 1987, Meiburg & Homsy 1988 and a few other authors). We need to keep in mind, however, a fundamental difference: all of the simulations reported here employed a spanwise domain width equal to the linearly most unstable wavelength, whereas in the immiscible experiments performed by the above authors the ratio of spanwise domain width to most unstable wavelength was not restricted. Clearly, the present

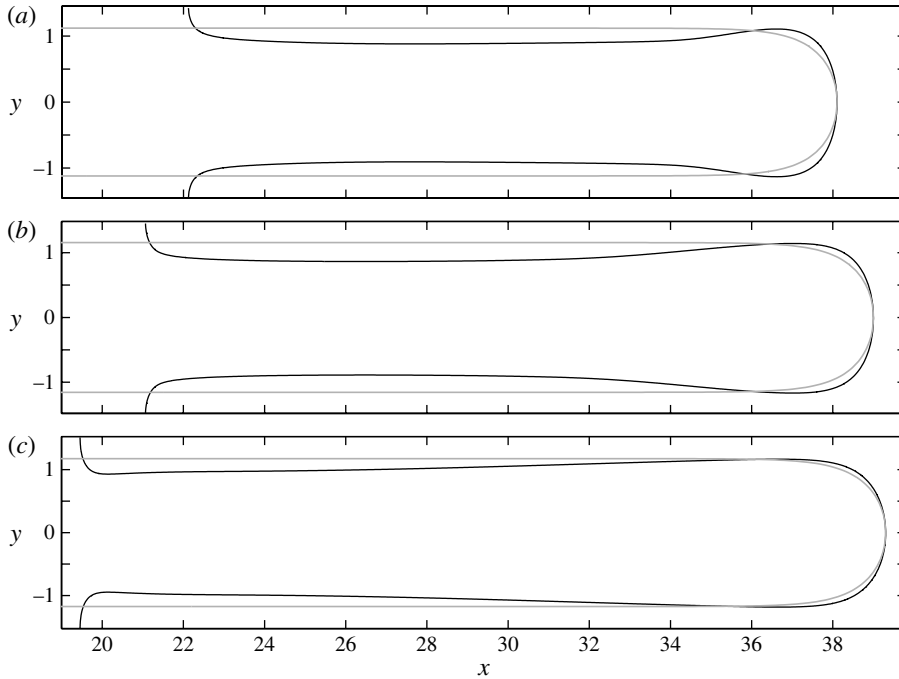


FIGURE 25. Comparison of the $c = 0.5$ contour at $t = 20$ (black) at the cell centre for $M = 3$ and (a) $Pe = 1000$, (b) 2000 and (c) 5000, with Pitts' relation (grey). For larger Péclet values, the miscible finger tip shape approaches Pitts' result.

simulation-based research will have to be extended to other domain widths in future, in order to explore the influence of this parameter. Using domain widths larger than the most unstable wavelength may promote a tip-splitting mechanism such as the one observed by Tan & Homsy (1988) for Darcy flows. While tip-splitting in miscible (immiscible) flows becomes more prominent for larger Péclet (capillary) numbers, this is not the case for the longitudinal, inner splitting observed here. For large Pe , the diffusive transport of resident fluid from the wall to the cell centre occurs more slowly, thereby delaying the inner splitting. We remark that it is not clear whether or not the inner splitting can also appear in immiscible flows. To our knowledge, it has not been observed yet, which may indicate that surface tension will always prevent the transport of resident, more viscous fluid to the cell centre.

Pitts (1980) provides an empirical relation for the finger tip shape, which gives very good agreement with experimental data for immiscible flows:

$$\exp\left(\frac{\pi x}{2m}\right) \cos\left(\frac{\pi y}{2m}\right) = 1. \quad (7.1)$$

Here m indicates the constant dimensionless finger width. Figures 25 and 26 compare the finger tip shape obtained from the present Navier–Stokes simulations with Pitts' analytical relation. For the sake of this comparison, m in his relation is set equal to the m_2 -value discussed above. For increasing Péclet numbers and viscosity ratios, the finger tip is seen to become less bulbous and increasingly similar to the shape provided by Pitts' relation. We remark that if we evaluate the overall finger shape

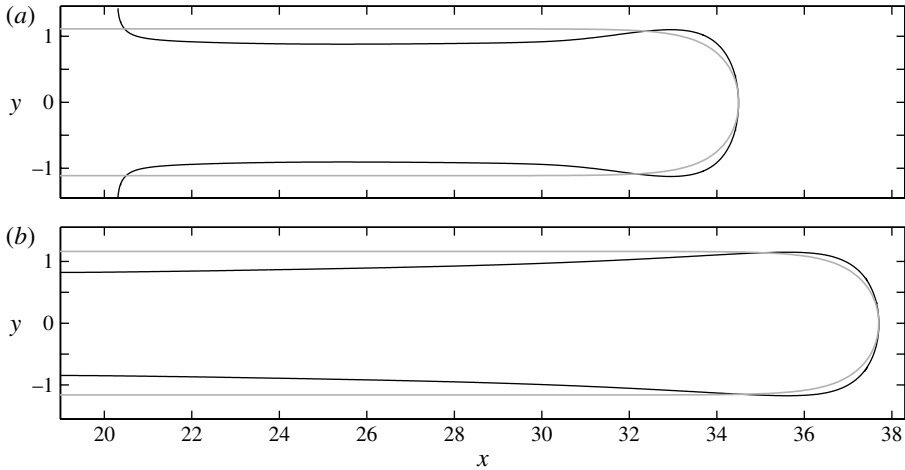


FIGURE 26. Comparison of the $c = 0.5$ contour at $t = 20$ (black) at the cell centre for $Pe = 1000$ and (a) $M = 3$ and (b) $M = 4$ with Pitts' relation. As the viscosity contrast increases, the miscible finger shape becomes increasingly similar to Pitts' relation.

based on gap-averaged concentration profiles rather than cell centre ones, the above qualitative observations remain valid.

8. Comparison with Darcy's law

To date, most computational investigations of Hele-Shaw displacements have been based on the gap-averaged Darcy's law (Bear 1972; Homsy 1987). Very recently, however, linear stability analyses based on the three-dimensional Stokes equations have begun to investigate the range of validity of Darcy's law for miscible displacement processes in Hele-Shaw cells. Specifically, the work by Goyal & Meiburg (2006) indicates that Darcy-based dispersion relations agree with their Stokes-based counterparts only for moderate values of Pe and M . Here, we will explore how well nonlinear processes can be captured by Darcy's law. Towards this end, we will focus on the displacement for $(M, Pe) = (3, 1000)$ at $t = 20$. A perspective view of the resulting finger is shown in figure 4.

Darcy's law is strictly valid for Hele-Shaw flows only if both the viscosity and the density are constant, and if inertial effects are negligible. Under these conditions, the flow is parallel to the walls everywhere and of Poiseuille type, so the flow direction is independent of the z -coordinate. The two-dimensional, gap-averaged velocity field is then governed by

$$(u, v) = -\frac{1}{12\mu} \left(\frac{\partial p}{\partial x}, \frac{\partial p}{\partial y} \right). \quad (8.1)$$

Due to the two-dimensional nature of the gap-averaged velocity field, only the z -component of the vorticity is non-zero, whereas both the streamwise and the spanwise vorticity components vanish. As we saw earlier in §5, a streamwise vorticity quadrupole structure plays an important role in promoting the inner splitting mechanism, so that it does not come as a surprise that this phenomenon had not been observed in Darcy-based simulations.

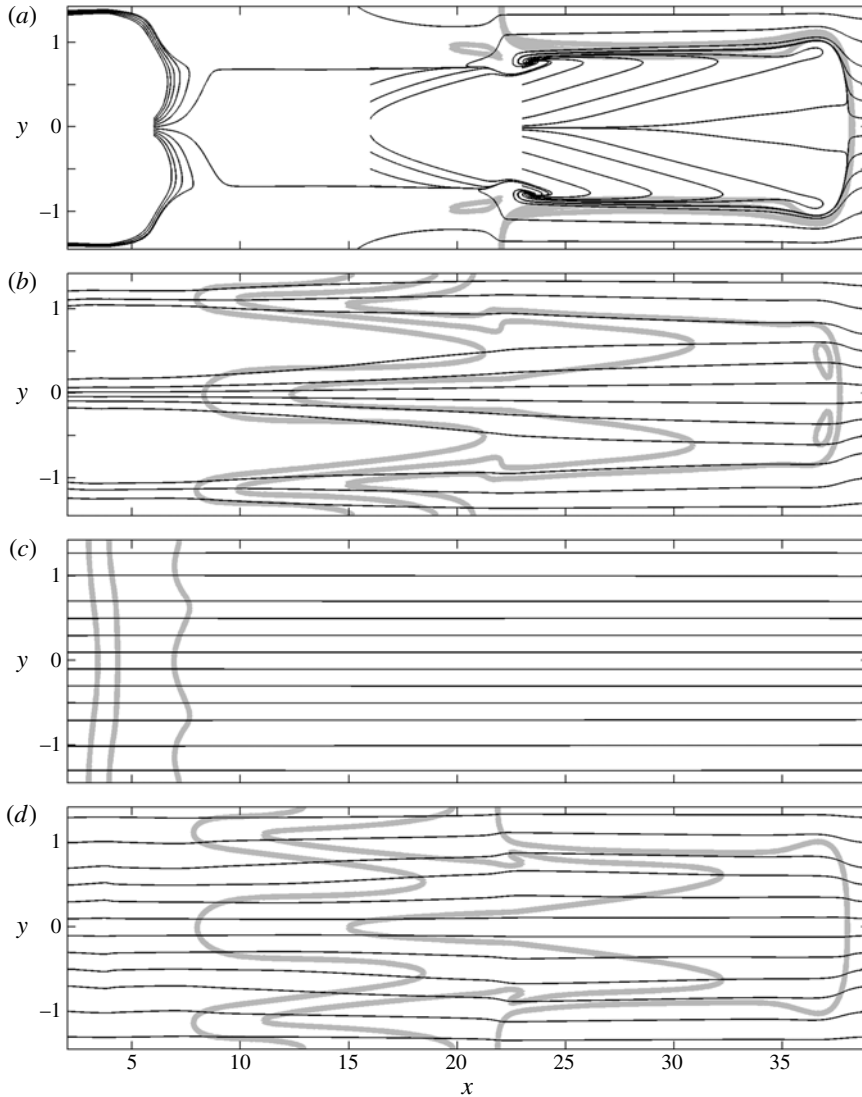


FIGURE 27. Lines tangential to the u, v -velocity field (black) in the reference frame moving with the finger tip. Shown are different z -levels: (a) the centre symmetry plane $z = 0$, (b) $z = 0.25$, (c) one grid spacing away from the wall. The grey lines indicate the $c = 0.3, 0.5$ and 0.7 contour levels. The direction of the velocity field is seen to vary strongly with z . (d) Streamlines showing the direction of the gap-averaged u, v -velocity field. The grey gap-averaged concentration contours correspond to the levels $c = 0.3, 0.5$ and 0.7 .

Figure 27 indicates the direction of the u, v -velocity field in black, in the reference frame moving with the finger tip, at three different z -levels. Superimposed in grey are the $c = 0.3, 0.5$ and 0.7 concentration contours. Figure 27(a) demonstrates the effect discussed above, namely streamlines coming from the right crossing the $c = 0.5$ interface at the finger tip, thereby transporting resident fluid into the finger. By comparing figures 27(a), 27(b) and 27(c), we recognize a strong dependence of the velocity direction field on the z -coordinate, indicating that the flow is far from

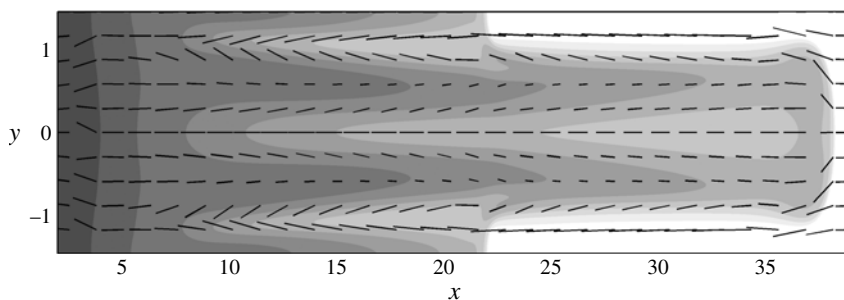


FIGURE 28. Velocity field in a moving reference frame as predicted by Darcy's law, along with gap-averaged concentration contours in continuous grey shading.

Poiseuille in nature. The streamlines of the gap-averaged velocity field, shown for comparison in figure 27(*d*), are qualitatively different from the directional fields of figure 27(*a–c*).

Figure 28 shows the velocity field calculated from Darcy's law in a moving reference frame in black along with continuous grey shading of the gap-averaged concentration contours. This velocity field was calculated by gap-averaging the pressure and viscosity fields of the DNS solution and using (8.1).

9. Conclusions

To our knowledge, the current investigation represents the first analysis of miscible Hele-Shaw displacements based on three-dimensional Navier–Stokes simulations. Our study primarily focuses on the properties of the quasisteady fingers as a function of the Péclet number and viscosity ratio, and on the subsequent instability of such fingers. The simulations show that the quasisteady tip velocity increases for larger values of the Péclet number and higher viscosity ratios. In general, the spanwise finger width varies along the streamwise direction, and attains its maximum value near the tip. Similarly, the finger thickness in the gap direction varies along the streamwise direction as well, so that the film of resident fluid left behind on the wall decreases in thickness towards the finger tip.

Along the entire length of the finger, resident fluid is convected from the wall towards the centre of the gap in the cross-gap symmetry plane of the finger, while injected fluid is transported laterally away from the finger centre within the mid-gap plane. These convective mechanisms owe their existence to a streamwise vorticity quadrupole along the length of the finger. Eventually, they result in the emergence of a longitudinal, inner splitting phenomenon some distance behind the tip that had not been reported previously. This inner splitting mechanism, which leaves the tip largely intact, is fundamentally different from the tip-splitting mechanism that has been known for some time (Tan & Homsy 1988). Since the cross-gap velocity and streamwise vorticity represent integral components of the inner splitting mechanism, it is believed that the inner splitting phenomenon cannot be reproduced on the basis of gap-averaged equations. Furthermore, the Navier–Stokes simulations show that the flow direction varies significantly in the cross-gap direction, which is at odds with the assumption of local Poiseuille flow. These observations draw attention to the limitations of Darcy's law when it comes to modelling Hele-Shaw displacements.

It was furthermore observed that the role of the Péclet number in miscible displacements does not correspond in all respects to that of the capillary number

in immiscible flows. The increase in the tip velocity for larger Péclet numbers corresponds to the trend for larger capillary numbers in immiscible flows. However, the increase in width observed for larger Péclet numbers is in contrast to immiscible flows, which display narrower fingers for larger capillary numbers. Similarly, while larger Péclet numbers delay inner splitting events, higher capillary numbers are known to promote tip-splitting. Interestingly, larger Péclet numbers have been found to result in earlier tip-splitting in miscible displacements, so that the Pe -value influences tip-splitting and inner splitting in opposite ways. Hence we expect the potential competition between inner and tip-splitting in wider Hele-Shaw cells to depend strongly on the value of this parameter.

There is some experimental evidence for the inner splitting mechanism observed here, both in the gravitationally driven Hele-Shaw flows of Wooding (1969) and in the capillary tube experiments of Petitjeans & Maxworthy (1996), as well as in preliminary unstable Hele-Shaw displacements by Tony Maxworthy (personal communication). Nevertheless, there is a clear need for further experiments and/or simulations before direct, quantitative comparisons can be undertaken.

The authors thank Dr Balakrishnan Selvam for his help in generating the Navier–Stokes solver, and Professors T. Maxworthy and G. Homsy for helpful discussions. High-performance computing support was received through the California NanoSystems Institute under grant NSF CHE-0321368, and through the Community Surface Dynamics Modelling System (CSDMS) facility at the University of Colorado in Boulder. We would like to thank CSDMS director Professor James Syvitski and the technical staff at CSDMS for their support. E.M. acknowledges financial support through NSF grant CBET-0651498, DOE grant DE-FG02-08ER15991, and from the Petroleum Research Fund, administered by the American Chemical Society, under grant 45175-AC9. R.M.O would like to thank the CAPES Foundation in Brazil and the Fulbright program for financial support through grants BEX 2615/06-1 and IIE 15073695.

REFERENCES

- AUBERTIN, A., GAUTHIER, G., MARTIN, J., SALIN, D. & TALON, L. 2009 Miscible viscous fingering in microgravity. *Phys. Fluids* **21**, 054107.
- BEAR, J. 1972 *Dynamics of Fluids in Porous Media*. American Elsevier.
- CHEN, C.-Y. & MEIBURG, E. 1996 Miscible displacements in a capillary tube. Part 2. Numerical simulations. *J. Fluid Mech.* **326**, 57–90.
- CHUOKE, R. L., VAN MEURS, P. & VAN DER POEL, C. 1959 The instability of slow, immiscible, viscous liquid–liquid displacements in permeable media. *Trans. AIME* **216**, 188–194.
- DEMUTH, R. & MEIBURG, E. 2003 Chemical fronts in Hele-Shaw cells: linear stability analysis based on the three-dimensional Stokes equations. *Phys. Fluids* **15** (3), 597–602.
- FERNANDEZ, J., KUROWSKI, P., PETITJEANS, P. & MEIBURG, E. 2002 Density-driven unstable flows of miscible fluids in a Hele-Shaw cell. *J. Fluid Mech.* **451**, 239–260.
- FERZIGER, J. H. & PERIĆ, M. 2002 *Computational Methods for Fluid Dynamics*. Springer.
- GOYAL, N. & MEIBURG, E. 2004 Unstable density stratification of miscible fluids in a vertical Hele-Shaw cell: influence of variable viscosity on the linear stability. *J. Fluid Mech.* **516**, 211–238.
- GOYAL, N. & MEIBURG, E. 2006 Miscible displacements in Hele-Shaw cells: two-dimensional base states and their linear stability. *J. Fluid Mech.* **558**, 329–355.
- GOYAL, N., PICHLER, H. & MEIBURG, E. 2007 Variable-density miscible displacements in a vertical Hele-Shaw cell: linear stability. *J. Fluid Mech.* **584**, 357–372.

- GRAF, F., MEIBURG, E. & HÄRTEL, C. 2002 Density-driven instabilities of miscible fluids in a Hele-Shaw cell: linear stability analysis of the three-dimensional Stokes equations. *J. Fluid Mech.* **451**, 261–282.
- GRESHO, P. & SANI, R. 1987 On pressure boundary conditions for the incompressible Navier–Stokes equations. *Intl J. Numer. Methods Fluids* **7**, 1111–1145.
- HILL, S. 1952 Channeling in packed columns. *Chem. Engng Sci.* **1**, 247–253.
- HOMSY, G. M. 1987 Viscous fingering in porous media. *Annu. Rev. Fluid Mech.* **19**, 271–311.
- JIANG, G.-S. & PENG, D. 2000 Weighted ENO schemes for Hamilton–Jacobi equations. *SIAM J. Sci. Comput.* **21** (6), 2126–2143.
- KIM, J. & MOIN, P. 1985 Application of a fractional-step method to incompressible Navier–Stokes equations. *J. Comput. Phys.* **59**, 308–323.
- KOPF-SILL, A. R. & HOMSY, G. M. 1987 Narrow fingers in a Hele-Shaw cell. *Phys. Fluids* **30**, 2607–2609.
- LAJEUNESSE, E., MARTIN, J., RAKOTOMALALA, N. & SALIN, D. 1997 3D instabilities of miscible displacements in a Hele-Shaw cell. *Phys. Rev. Lett.* **79** (26).
- MARTIN, J., RAKOTOMALALA, N. & SALIN, D. 2002 Gravitational instability of miscible fluids in a Hele-Shaw cell. *Phys. Fluids* **14** (2).
- MCLEAN, J. W. & SAFFMAN, P. G. 1981 The effect of surface tension of the shape of fingers in a Hele-Shaw cell. *J. Fluid Mech.* **102**, 261–282.
- MEIBURG, E. & HOMSY, G. M. 1988 Nonlinear unstable viscous fingers in Hele-Shaw flows. Part II. Numerical simulation. *Phys. Fluids* **31**, 429–439.
- OLIVEIRA, RAFAEL M. 2012 Three-dimensional DNS simulations of confined miscible flows. PhD thesis, UCSB.
- OSHER, S. & FEDKIW, R. 2003 *Level Set Methods and Dynamic Implicit Surfaces*. Springer.
- PACHECO, P. 1997 *Parallel Programming with MPI*. Morgan Kaufmann.
- PATERSON, L. 1985 Fingering with miscible fluid in a Hele-Shaw cell. *Phys. Fluids* **28** (1).
- PETITJEANS, P. & MAXWORTHY, T. 1996 Miscible displacements in capillary tubes. Part 1. Experiments. *J. Fluid Mech.* **326**, 37–56.
- PITTS, E. 1980 Penetration of fluid into a Hele-Shaw cell. *J. Fluid Mech.* **97**, 53–64.
- QIN, J. & NGUYEN, D. T. 1998 A tridiagonal solver for massively parallel computers. *Adv. Engng Software* **29**, 395–397.
- RAI, M. M. & MOIN, P. 1991 Direct simulations of turbulent flow using finite-difference schemes. *J. Comput. Phys.* **96** (1), 15–53.
- RAKOTOMALALA, N., SALIN, D. & WATZKY, P. 1997a Fingering in 2D parallel viscous flow. *J. Phys. II France* **7** (1967).
- RAKOTOMALALA, N., SALIN, D. & WATZKY, P. 1997b Miscible displacement between two parallel plates: BGK lattice gas simulations. *J. Fluid Mech.* **338**, 277–297.
- SAFFMAN, P. G. & TAYLOR, G. I. 1958 The penetration of a fluid into a porous medium or Hele-Shaw cell containing a more viscous liquid. *Proc. R. Soc. Lond. Ser. A* **245**, 312–329.
- SCHAFROTH, D., GOYAL, N. & MEIBURG, E. 2007 Miscible displacements in Hele-Shaw cells: nonmonotonic viscosity profiles. *Eur. J. Mech. B/Fluids* **26**, 444–453.
- TAN, C. T. & HOMSY, G. M. 1986 Stability of miscible displacements in porous media: rectilinear flow. *Phys. Fluids* **29** (11), 3549–3556.
- TAN, C. T. & HOMSY, G. M. 1988 Simulation of nonlinear viscous fingering in miscible displacement. *Phys. Fluids* **31** (6), 1330–1338.
- VANAPARTHY, S. H. & MEIBURG, E. 2008 Variable density and viscosity, miscible displacements in capillary tubes. *Eur. J. Mech. B/Fluids* **27**, 268–289.
- WOODING, R. A. 1969 Growth of fingers at an unstable diffusing interface in a porous medium or Hele-Shaw cell. *J. Fluid Mech.* **39**, 477–495.
- ZENG, J., YORTSOS, Y. C. & SALIN, D. 2003 On the Brinkman correction in unidirectional Hele-Shaw flows. *Phys. Fluids* **15** (12).